Ultrahigh-Net-Bitrate 363 Gbit/s PAM-8 and 279 Gbit/s Polybinary Optical Transmission Using Plasmonic Mach-Zehnder Modulator

Qian Hu, *Member, IEEE*, Robert Borkowski, *Member, IEEE*, Yannick Lefevre, Junho Cho, *Senior Member, IEEE*, Fred Buchali, René Bonk, Karsten Schuh, Eva De Leo, Patrick Habegger, Marcel Destraz, Nino Del Medico, Hamit Duran, Valentino Tedaldi, Christian Funck, Yuriy Fedoryshyn, Juerg Leuthold, Wolfgang Heni, Benedikt Baeuerle, and Claudia Hoessbacher

(Post-Deadline Paper)

***Abstract*—We summarize our experimental exploration of the capabilities of an ultrabroad-bandwidth plasmonic Mach-Zehnder modulator (MZM), in an intensity modulation and direct detection (IM/DD) system for short-reach optical transmission up to 10 km. We study modulation, transmission, and reception of ultrahigh-symbol-rate (up to 304 GBd) multi-level optical signals with two different signaling schemes: pulse amplitude modulation (PAM), with up to 8 amplitude levels and partial-response-encoded binary (polybinary) modulation with memory length up to 4. By mapping the performance to a concatenated soft-decision (SD) and hard-decision (HD) forward error correction (FEC) coding scheme, a net bitrate of 363.4 Gbit/s is possible with PAM-8 signaling and 279.0 Gbit/s with tetrabinary (polybinary) signaling after 10 km standard single-mode fiber transmission. Considering an HD-only coding scheme, a net bitrate of 318.0 Gbit/s is possible with PAM-6 and 277.1 Gbit/s with tetrabinary.**

***Index Terms*—Intensity modulation and direct detection, plasmonic Mach-Zehnder modulator, ultrahigh-speed optical transmission.**

Manuscript received January 20, 2022; revised April 26, 2022; accepted April 27, 2022. Date of publication May 3, 2022; date of current version May 25, 2022. The work of Yannick Lefevre was supported by the Flemish Government funding Agency VLAIO through the SPIC Project under Grant HBC.2020.2197. *(Corresponding author: Qian Hu.)*

Qian Hu, Robert Borkowski, and René Bonk are with Nokia Bell Labs, 70469 Stuttgart, Germany (e-mail: qian.hu@nokia-bell-labs.com; robert.borkowski@nokia-bell-labs.com; rene.bonk@nokia-bell-labs.com).

Yannick Lefevre is with Nokia Bell Labs, 2018 Antwerp, Belgium (e-mail: yannick.lefevre@nokia-bell-labs.com).

Junho Cho is with Nokia Bell Labs, Murray Hill, NJ 07974 USA (e-mail: junho.cho@ieee.org).

Fred Buchali and Karsten Schuh are with Nokia, Network Infrastructure – Optical Networks division, 70469 Stuttgart, Germany (e-mail: fred.buchali@nokia.com; karsten.schuh@nokia.com).

Eva De Leo, Patrick Habegger, Marcel Destraz, Nino Del Medico, Hamit Duran, Valentino Tedaldi, Christian Funck, Wolfgang Heni, Benedikt Baeuerle, and Claudia Hoessbacher are with Polariton Technologies Ltd., 8803 Rüschlikon, Switzerland (e-mail: eva@polariton.ch; patrick@polariton.ch; marcel.destraz@polariton.ch; nino@polariton.ch; hamit@polariton.ch; valentino.tedaldi@polariton.ch; christianf@polariton.ch; wolfgang@polariton.ch; benedikt@polariton.ch; claudia@polariton.ch).

Yuriy Fedoryshyn and Juerg Leuthold are with ETH Zürich, Institute of Electromagnetic Fields (IEF), 8092 Zürich, Switzerland (e-mail: yuriy.fedoryshyn@ief.ee.ethz.ch; leuthold@ethz.ch).

Color versions of one or more figures in this article are available at https://doi.org/10.1109/JLT.2022.3172246.

Digital Object Identifier 10.1109/JLT.2022.3172246

I. Introduction

THE enormous expansion of cloud computing is currently driving a rapid growth of data center traffic. In response, future standards for short-reach datacenter interconnects (DCIs) aim at beyond-800G optics (e.g., 1.6TbE [1]). Low complexity solutions based on intensity modulation and direct detection (IM/DD) are preferred due to demanding transceiver cost targets in datacom, but at the same time lanes at 200 Gbit/s and beyond are needed to meet future bandwidth demands of short-reach DCIs [2], [3]. To support high-speed optical signal modulation in next generation short-reach systems, one of the key elements is an optical modulator with a large electro-optical (EO) bandwidth and a small footprint. The former characteristic is necessary to keep a small number of parallel lanes when increasing the total data rate of the optical interface, thus enabling low complexity chips with low power consumption; the latter is essential to achieve a high degree of integration and a high faceplate density in case of pluggable form factors.

Optical signal modulation can be realized by direct current modulation of a light source (e.g., modulating drive current of a directly modulated laser, DML) [4]–[6]), or by using a modulator external to the light source [7]–[15]. Operations of optical modulators are often based on three types of electro-optic (EO) effects: carrier plasma dispersion effect [7], electro-absorption effect [8]–[10] and Pockels effect [11]–[15]. Thanks to the advancement of laser and modulator technologies in recent years, EO bandwidths exceeding 100 GHz have been shown to be achievable using different types of devices, such as DMLs [4], [5], electro-absorption modulators (EAMs) [8], or modulators based on Pockels effect [12]–[15]. Especially modulators based on Pockels effect can support not only a large EO bandwidth but also a broad optical bandwidth, which makes them well suited for WDM applications. Such modulators typically require active section with a length of a few millimeters [12] or more to achieve desired modulation depth. Plasmonic modulators combine Pockels-type materials with plasmonics, allowing to improve the modulation efficiency significantly and shorten length of an active section to micrometers [13]. With

micron-scale dimensions, plasmonic modulators allow for a dense array of optical channels with a small footprint, which makes them promising solutions for future highly integrated high-speed optical transmitters.

A 200 Gbit/s PAM-4 transmission [14], and a 222 GBd on-off keying (OOK) transmission [15] were successfully demonstrated using a plasmonic Mach-Zehnder modulator (MZM). In our recent work [16], we reported on an almost doubled (432 Gbit/s) line rate and a 37% increased (304 GBd) symbol rate compared to [15], using the same type of modulator. Two types of multi-level signals were employed to demonstrate the capabilities of plasmonic modulators in terms of high-speed intensity modulation: (a) m-level pulse amplitude modulation (PAM-m) signals, which enable transmission at higher information rates compared to conventional binary (PAM-2) signals by increasing the number of amplitude levels; and (b) partial-response-encoded binary (polybinary) signals created with filters of order n [17], [18] (n+1-symbol-long memory), which result in spectral shaping of encoded signals, consequently allowing for transmission at higher symbol rates compared to conventional binary signals and use of a limited-complexity decoder on the receiver side. After 10 km standard single mode fiber (SSMF), a net bitrate of 350.4 Gbit/s was demonstrated based on a 144 GBd PAM-8 signal, while a symbol rate of 304 GBd was demonstrated with tetrabinary[1] modulation, yielding a net bitrate of 274.0 Gbit/s.

In this paper, we extend our previous work [16] and present the following new results: (1) measurements based on two new modulation formats: PAM-3 and PAM-6 with non-uniform amplitude levels probability, based on time-serialized 8-ary quadrature amplitude modulation (QAM-8) and QAM-32, respectively, are included; (2) two forward error correction (FEC) coding schemes: (i) soft-decision (SD) tail-biting spatially-coupled (SC) low-density parity check (LDPC) codes concatenated with a hard-decision (HD) Bose-Chaudhuri-Hocquenghem (BCH) code, and (ii) HD staircase codes, are employed for computation of net bitrates, allowing us to demonstrate even higher net bitrates compared to the ones reported previously in [16]. Using the concatenated FEC coding scheme, a net bitrate of 363.4 Gbit/s is achieved after 10 km SSMF transmission using PAM-8 signaling at a symbol rate higher than 140 GBd, and 279.0 Gbit/s with tetrabinary signaling at a symbol rate higher than 300 GBd.

The remainder of this paper is organized as follows: Section II describes the plasmonic MZM under test and its relevance for ultrahigh-speed optical signal modulation. Section III provides details on the IM/DD experimental setup used for the demonstration, explains the studied modulation formats and FEC codes, and outlines the digital signal processing (DSP) steps performed in the transmitter and the receiver. The experimental results are presented in Section IV, followed by analyses comparing net bitrates obtianed with different combinations of modulation formats and FEC coding schemes.

[1]In our work we adopt the following systematic naming convention for polybinary modulation obtained after n iterations of duobinary filtering: Greek prefix for a filter memory length [18] (i.e., filter order n plus one) + Latin prefix for a number of amplitude levels of the source modulation + 'ary'. For instance, *tetrabinary* refers to a PAM-2 (*binary*) modulation passed through a filter with a memory length of four (*tetra*). Nonetheless, in the literature other names, such as 'quatrobinary' [19], '3rd-order duobinary' [20] can be found. Names referring to the system class [18] , or 'duo-PAM-m', especially in case of source modulation with a higher number of amplitude levels, are also in use.

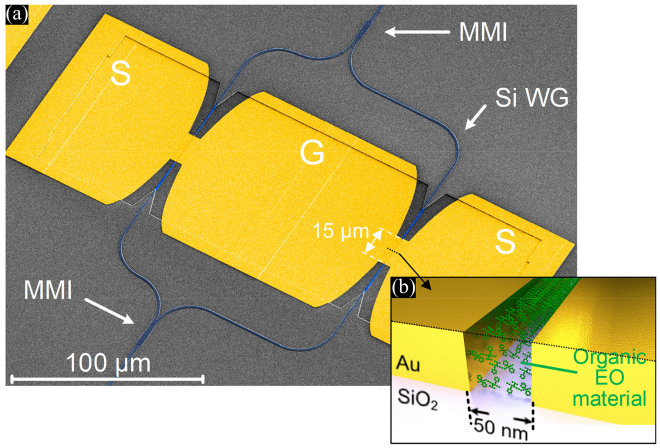

Fig. 1. (a) Top view image of the plasmonic-organic hybrid MZM. (b) Cross-section of the metal-insulator-metal slot waveguide, where surface plasmon polaritons propagate along the interfaces.

II. Plasmonic MZM

Fig. 1(a) shows a photomicrograph of the surface of the plasmonic-organic hybrid (POH) MZM. The MZM is integrated on a silicon-on-insulator wafer, where passive silicon photonics (SiPh) components, such as waveguides, splitters/combiners, grating couplers or thermo-optic phase shifters, can be built using standard SiPh technology. Active components of the modulator, namely two phase shifters, are built based on metal-insulator-metal (MIM) slot waveguides [21]. A generic cross-section of a 50-nm-wide MIM slot waveguide is illustrated in Fig. 1(b) [22]. The metal electrodes of the waveguide have twofold functions: (1) high frequency electrodes for the electrical driving signal, and (2) guiding structure for the optical mode. The slot between the metal electrodes is filled with an organic EO material [23]. Surface plasmon polaritons, which propagate along the metal-insulator interfaces, lead to tight spatial confinement of the optical field. When a voltage is applied across the slot, the refractive index of the organic material is changed due to the Pockels effect [24], altering optical phase of the passing light. Two MIM slot waveguides are connected using silicon waveguides, forming an interferometric structure of the MZM. The optical mode is coupled from and to the slot waveguide via a tapered silicon ridge waveguide.

Electrical and optical fields are tightly confined and overlap nearly perfectly in the MIM slot waveguide [25], resulting in a very high modulation efficiency per unit length. Consequently, the active length of the MIM slot waveguide can be as short as 5 μm to 15 μm [15]. There are two benefits of such short active length: (1) walk-off between electrical and optical waves is negligible; (2) the micron-scale dimensions of the metal electrodes lead to a small parasitic RC constant, allowing high EO bandwidth of the modulator. The electro-optic response of

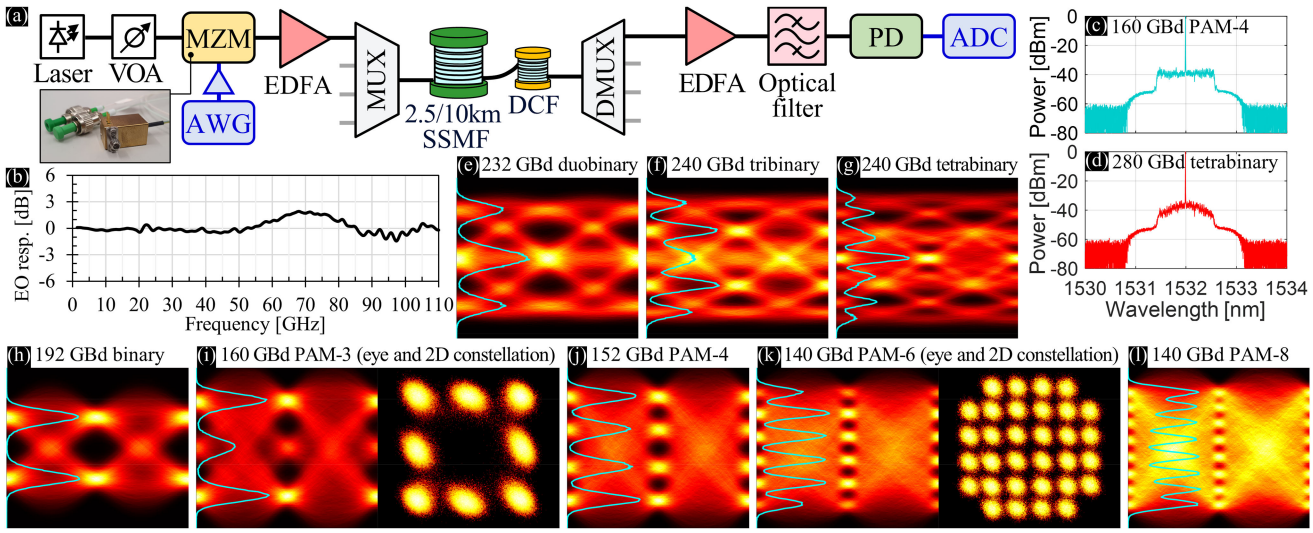

Fig. 2. (a) Schematic of the experimental setup. (b) EO response of the packaged plasmonic MZM under test. (c, d) Optical spectra of the transmitted signals. (e-g) Polybinary modulation eye diagrams. (h-l) PAM eye diagrams and constellation diagrams reconstructed from two consecutive symbols (for 2D demodulation of PAM-3 and PAM-6). Signals (e-l) are captured at the output of the equalizer.

an unpackaged modulator of this type shows merely 1 dB of attenuation at 500 GHz [26]. The active organic material of the plasmonic MZM allows for operation in the wavelength range spanning across entire conventional telecom wavelength range: 1.2 μm to 1.6 μm [27]. However, grating couplers at the input and output of the modulator will limit the optical bandwidth. The device under test (DUT) has an operating wavelength range from 1500 nm to 1555 nm. With a different coupler design, its operation in O band, around zero-dispersion wavelength, could also be possible, thus promising ultrafast transmission also over dispersion-uncompensated fibers with kilometers of fiber length.

III. Ultrahigh-Net-Bitrate Transmission Experiment

The DUT is evaluated in an experimental IM/DD setup with up to 10 km fiber to demonstrate its capability to support ultrahigh-symbol-rate multi-level optical modulation.

A. IM/DD Experimental Testbed

The IM/DD system used in this experiment is schematically illustrated in Fig. 2(a). The plasmonic MZM (the DUT) is packaged into a non-hermetic gold box and fitted with a 1 mm connector, as shown in a photograph in Fig. 2(a). Wire bonds are used to establish high-frequency electrical interfaces to the photonic integrated circuit.

The packaged DUT has a 3 dB bandwidth well exceeding 110 GHz, shown in Fig. 2(b), and exhibits even slight peaking around 70 GHz. Static V_π of the DUT is 8.3 V. Since the modulator constitutes a purely capacitive load, the double of the 50-Ω-measured voltage is effectively acting on the pads of the modulator when connected to a 50-Ω-output signal source. The fiber-to-fiber loss of the DUT is 18.2 dB at 1532 nm: on-chip loss, which includes all losses between two fiber-to-chip interfaces except for fiber-to-chip coupling losses, is around 10 dB, while each grating coupler contributes further 4 dB loss. The static extinction ratio was measured to be >28 dB.

The electrical signal fed into the DUT is generated from a 256 GSa/s arbitrary waveform generator (AWG) with 65 GHz 3-dB analog bandwidth, followed by an 11 dB driver amplifier with 70 GHz bandwidth, producing driving voltage up to 2.8 V_{pp} if measured with a 50-Ω-matched instrument. The actual voltage acting on the modulator is doubled due to the purely capacitive nature of the modulator. A laser source emitting at 1532 nm provides an optical carrier with optical power up to 10 dBm launched into the DUT. The output of the DUT is connected to a booster-type erbium-doped fiber amplifier (EDFA) to compensate for the insertion loss of the DUT, and is followed by a programmable optical filter, which emulates a channel multiplexer with a 2 nm fourth-order super-Gaussian transfer function and also filters amplified spontaneous emission (ASE) noise from the EDFA. The optical power launched to the fiber is 9.5 dBm. A SSMF of 2.5 km or 10 km is used in the experiment. The dispersion accumulated in the SSMF is compensated by a matched dispersion compensating fiber (DCF). At the receiver, another optical filter, emulating a channel demultiplexer, is used. The received optical signal is pre-amplified with another EDFA, passes through a 1.5 nm optical filter for ASE noise suppression and is detected using a 100 GHz *p-i-n* photodetector (PD). The input power to the PD is 6.5 dBm. The photocurrent is sampled by a free-running 256 GSa/s analog-to-digital converter (ADC) with an 84 GHz anti-aliasing brick-wall filter.

B. Modulation Formats and Digital Signal Processing

Two types of multi-level signals are modulated on the optical carrier using the plasmonic MZM: *m*-level PAM signals (PAM-*m*, $m \in \{2,3,4,6,8\}$) and polybinary signals created with filters of order *n*, $n \in \{1,2,3\}$. The employed modulation formats are summarized in Table I. Fig. 2(h-l) show examples of eye

TABLE I
DETAILS OF STUDIES MODULATION FORMATS

Modulation format	Encoder filter impulse response[a]	Entropy H [bit/sym]	Amplitude levels	Probability of each amplitude level	Symbol labeling[b]	Decoding[c]
PAM-2	1	1	2	½ · [1 1]	Gray code in 1D	1D symbol-by-symbol
PAM-3	1	1.5	3	⅛ · [3 2 3]	Gray code in 2D	2D symbol-by-symbol QAM-(3×3), no center point
PAM-4	1	2	4	¼ · [1 1 1 1]	Gray code in 1D	1D symbol-by-symbol
PAM-6	1	2.5	6	1/16 · [2 3 3 3 3 2]	Quasi-SU mapping [28]	2D symbol-by-symbol QAM-(6×6), no corner points
PAM-8	1	3	8	⅛ · [1 1 1 1 1 1 1 1]	Gray code in 1D	1D symbol-by-symbol
Duobinary	$1 + z^{-1}$	1	3	¼ · [1 2 1]	Gray code in 1D	2-state BCJR
Tribinary	$1 + 2z^{-1} + z^{-2}$	1	5	⅛ · [1 2 2 2 1]	Gray code in 1D	4-state BCJR
Tetrabinary	$1 + 3z^{-1} + 3z^{-2} + z^{-3}$	1	9	1/16 · [1 2 1 2 4 2 1 2 1]	Gray code in 1D	8-state BCJR

[a]Impulse response 1 is equivalent to no filtering.
[b]Gray code is equivalent to natural labeling for binary signal; for polybinary, labeling is applied to the source binary modulation.
[c]Symbol-by-symbol decoding is performed in one (1D) or two (2D) dimensions by finding an ideal symbol with the smallest Euclidean distance to the symbol tuple in 1D or 2D constellation space. Symbol tuples are formed from consecutive nonoverlapping windows of equalized received symbols.

diagrams obtained at the output of the receiver equalizer after 2.5 km dispersion-compensated transmission for various PAM-m signals. PAM-3 and -6 signals are generated by transmitting each dimension of the corresponding constellation space of QAM-8 (3×3 grid with center point removed) and QAM-32 (6×6 grid with corner points removed) shown in Fig. 2(i,k) into two consecutive PAM symbols (timeslots). For PAM-2, -3, -4, -6, -8 signals, entropy H, is 1 bit/sym, 1.5 bit/sym, 2 bit/sym, 2.5 bit/sym and 3 bit/sym, respectively. For PAM-3 and -6 it is slightly lower (by ≈0.085 bit/sym) than the maximum possible entropy of $\log_2(m)$, necessitated by practical symbol mapping scheme (particularly, number of symbols jointly considered by the demapper).

To generate partial response polybinary signals with memory length n+1, a binary signal is convolved with an impulse response $(1 + z^{-1})^n$ [17]–[20]. The resulting signals have 2^n+1 discrete amplitude levels with non-uniform probability distribution (see Table I), corresponding to duobinary for n+1 = 2, tribinary for n+1 = 3 and tetrabinary for n+1 = 4. Fig. 2(e-g) show examples of eye diagrams obtained at the output of the receiver equalizer when employing polybinary signals. For all polybinary signals, the entropy is defined by the source modulation (binary) and thus remains fixed at 1 bit/sym. The advantage of polybinary signaling lies in its ability to perform spectral shaping, realized by a short, predefined correlation in time domain, which can be subsequently decoded using maximum likelihood detection with a small number of states. In our experiment, the correlation is induced by a digital filter of order n (i.e., a filter with n+1 taps), with tap coefficients obtained from expansion of the polynomial $(1 + z^{-1})^n$. In frequency domain this is equivalent to multiplication of the power spectrum by $|\cos(\pi f/R_s)|^{2n}$, with f being the frequency and R_s the symbol rate. The spectral compression induced by this filtering can be observed in the optical spectrum of 280 GBd tetrabinary signal in Fig. 2(d). Considering a bandwidth limited system, polybinary modulation can be used to achieve a higher symbol rate compared to conventional binary modulation. A higher n leads to stronger spectral shaping, thus less energy dissipation due to bandwidth limitation, which is beneficial to further increase symbol rate. However, it also leads to a rapid increase in the number of amplitude levels: for n+1 = 4, the number of amplitude levels is 9, while for n+1 = 5 it grows to 17, considerably increasing required signal-to-noise ratio (SNR). For this reason, cases of n+1>4 are not considered in this paper.

In the transmitter DSP, PAM and polybinary signals are resampled to 256 GSa/s, and pulse-shaped by a raised-cosine (RC) filter with a roll-off of 0.1. With spectral shaping, polybinary signals at >256 GBd can be generated by a 256 GSa/s AWG. For these signals, frequency components at >128 GHz are first removed before down-sampling to 256 GSa/s to avoid folding of the spectrum onto itself. Next, hardware-specific pre-emphasis is applied, which de-embeds the frequency response of the AWG and driver amplifier up to 72 GHz. The intrinsic response of the DUT is not compensated for, due to its >110 GHz EO bandwidth (Fig. 2(b)). The modulated optical signal has a 6 dB bandwidth of approximately 72 GHz after applying pre-emphasis.

In the receiver DSP, received signal is resampled to 2 samples/symbol (Sps) and filtered to remove out-of-band noise. For both PAM and polybinary signals, a T/2 spaced nonlinear feed-forward equalizer (FFE) concatenated with a T-spaced decision feedback equalizer (DFE) is applied. To demonstrate the highest possible data rate, we use an FFE with 301 taps in the linear (first) term, and polynomial kernels originating from a span of 41 samples for the second and third order terms. A DFE with 7 taps is concatenated at the output of the FFE. The equalizer targets an ideal multi-level signal. For polybinary signals, this ideal signal corresponds to the impulse response $(1 + z^{-1})^n$ applied at the transmitter to generate the polybinary signals. Potential phase drifts between the unsynchronized clocks of the transmitter and the receiver are compensated within the adaptive equalizer. After equalization, signals are decimated to 1 Sps.

Channel transition probability is then measured from the histogram of the equalized signal, based on which normalized generalized mutual information (NGMI) is computed. For PAM-2, -4 and -8, the NGMI metric is computed directly from the equalized signal assuming Gray labeling, while for PAM-3 and -6 signals, NGMI computation is performed in two dimensional signal space reconstructed from two consecutive

symbols, respectively based on QAM-8 with Gray labeling around the perimeter, and QAM-32 constellation with quasi-SU bit mapping [28, Fig. 15(a)]. Subsequently, symbol decisions are made by finding the reference symbol with minimum Euclidean distance, and the symbol is converted to its bit representation, from which BER can be computed.

For polybinary signals, a low-complexity Bahl-Cocke-Jelinek-Raviv (BCJR) algorithm with a small number of states equal to 2^n is applied to the equalized signal to decode a multi-level polybinary signal back to a binary sequence. The algorithm computes log-likelihood ratios (LLRs), assuming Gaussian channel model. The output LLRs are subsequently used for computation of the NGMI metric. BER is computed based on bit decisions which are made according to LLR signs.

C. Forward Error Correction Codes

To determine practically achievable net bitrates, we consider two different FEC coding schemes[2]: (i) SD and HD (SD+HD) concatenated coding, and (ii) HD-only coding.

For the SD+HD concatenated FEC coding scheme, we use tail-biting SC-LDPC codes for the inner SD code and a BCH code for the outer HD code. We construct the SC-LDPC codes by first creating 4-cycle-free protographs [29] whose degrees are optimized using the extrinsic information transfer (EXIT) chart analysis [30], and then lifting the protographs based on the approximate cycle extrinsic message degree (ACE) algorithm [31]. Such constructed codes have a good structure for application-specific integrated circuit implementation, excellent waterfall performance and a low error floor. In the concatenated coding scheme, the inner SC-LDPC codes of various code rates lower the BER to 10^{-5} after normalized min-sum decoding with up to 30 iterations in layered scheduling. Then, BCH(16383,16243,10) code, with a pre-FEC BER threshold of 1.3×10^{-5} is used to reach a post-FEC BER of 10^{-15}. This assumes that a long bit interleaver is placed between the inner and outer FEC decoders, as is common in optical communications standards to remove possible error bursts, so that the following outer BCH decoder can see a stationary channel with independent and identically distributed bit errors. Table II shows NGMI thresholds of these SD+HD concatenated FEC codes. To cover a wide range of NGMI values measured in the experiment, we further show in Table II the approximate NGMI thresholds for various codes that can be obtained by puncturing the rate-0.8750 LDPC code (thus the rate of the punctured codes is higher than 0.8750). Under random puncturing, these NGMI thresholds of the punctured codes can be estimated by using the information-theoretic approach described in [32]. Namely, given a rate-r mother code with an NGMI threshold of I, the NGMI threshold I_p of its punctured codes with rate r_p, $r_p > r$, is approximately determined from the relation $I_p/\ r_p = \ I/r$.

For the HD-only FEC coding scheme, we use a family of staircase codes constructed from four-error correcting BCH component codes [33, Table I]]. Their BER thresholds established with simulation, performing a maximum of eight decoding iterations over a binary symmetric channel (BSC), are shown in Table II for reference.

TABLE II
NGMI/BER THRESHOLDS FOR THE CONSIDERED FEC CODES

FEC code	Inner code rate [–]	Overall code rate[d] [–]	NGMI threshold [–]
SD[a]+HD concatenated[b]	0.7583	0.7519	0.8116
	0.7667	0.7602	0.8167
	0.7750	0.7684	0.8241
	0.7833	0.7766	0.8317
	0.7917	0.7850	0.8401
	0.8000	0.7932	0.8459
	0.8083	0.8014	0.8512
	0.8167	0.8098	0.8574
	0.8250	0.8180	0.8685
	0.8333	0.8262	0.8746
	0.8417	0.8345	0.8829
	0.8500	0.8428	0.8892
	0.8583	0.8510	0.8958
	0.8667	0.8593	0.9022
	0.8750 *	0.8676	0.9090
SD+HD concatenated[b] with punctured LDPC based on mother code *	0.8808	0.8733	0.9150
	0.8865	0.8790	0.9210
	0.8923	0.8848	0.9270
	0.8981	0.8905	0.9330
	0.9039	0.8962	0.9390
	0.9096	0.9019	0.9450
	0.9154	0.9077	0.9510
	0.9212	0.9134	0.9570
	0.9270	0.9191	0.9630
	0.9328	0.9248	0.9690
	0.9385	0.9306	0.9750
	0.9443	0.9363	0.9810
	0.9501	0.9420	0.9870
	0.9559	0.9477	0.9930
	0.9616	0.9535	0.9990
	–	Code rate [–]	BER threshold [–]
HD-only[c]	–	0.7500	2.12×10^{-2}
	–	0.8000	1.76×10^{-2}
	–	0.8123	1.62×10^{-2}
	–	0.8333	1.44×10^{-2}
	–	0.8571	1.25×10^{-2}
	–	0.8750	1.03×10^{-2}
	–	0.8889	9.29×10^{-3}
	–	0.9000	8.33×10^{-3}
	–	0.9091	7.54×10^{-3}
	–	0.9167	7.04×10^{-3}
	–	0.9412	4.70×10^{-3}

[a]Block length for LDPC is 30720 bits.
[b]Post-inner-FEC target BER$<10^{-5}$, post-outer-FEC target BER$<10^{-15}$.
[c]Post-FEC target BER$<10^{-15}$; block length is 46656 bits.
[d]The overall code for SD+HD FEC codes includes a 0.9915 rate BCH code.

IV. RESULTS AND ANALYSIS

The performance of the IM/DD system is evaluated in a wide range of symbol rates employing various PAM and polybinary modulation formats.

A. Performance Evaluation of PAM Signaling

For various PAM signals, the obtained NGMI, computed directly based on equalized symbols, and BER, computed from symbol decisions and their bit representations, are plotted as a

[2]These FEC schemes are different from those used in our previous work [16], where for (i) we considered DVB-S2 SD LDPC code family concatenated with a HD staircase code, while for (ii) a few different codes (KP4, G.975.1 and G.9804.2) were shown.

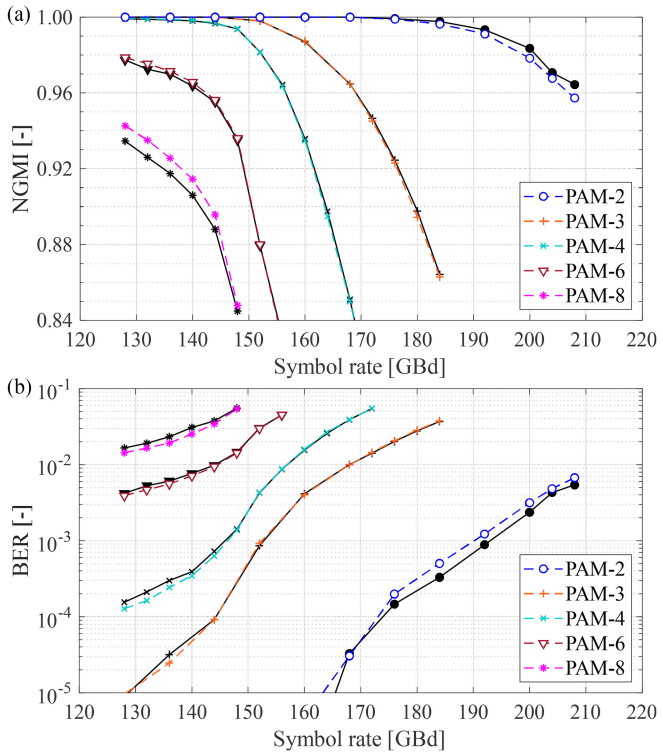

Fig. 3. (a) NGMI and (b) BER as a function of symbol rate for PAM after 2.5 km (dashed colored lines) and 10 km (black continuous lines) SSMF transmission.

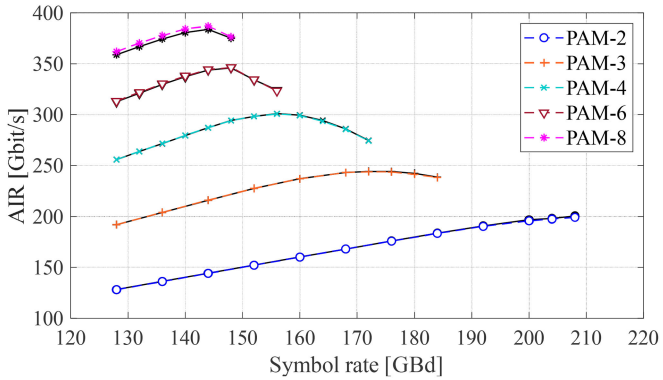

Fig. 4. AIR for PAM after 2.5 km (dashed colored lines) and 10 km (black continuous lines) SSMF transmission.

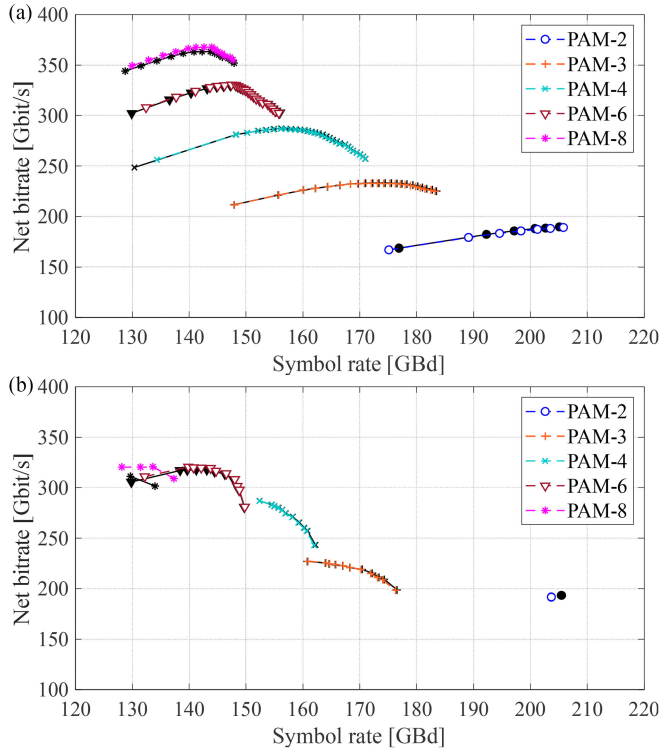

Fig. 5. Net bitrate achieved with: (a) SD+HD FEC and (b) HD-only FEC, as a function of symbol rate for PAM after 2.5 km (dashed colored lines) and 10 km (black continuous lines) SSMF transmission.

function of symbol rate in Fig. 3. Different markers are used to indicate the results obtained with different modulation formats. Results obtained after 2.5 km of compensated SSMF transmission are plotted in different colors with dashed lines, while results measured after 10 km of compensated SSMF are plotted with black continuous lines (in most cases superposed on colored lines). Back-to-back results, which overlap with 2.5 km results are not included for clarity of presentation, while 2.5 km and 10 km results very closely follow each other in majority of cases, showing a negligible penalty after dispersion-compensated fiber transmission. For brevity, we report only on the results after 10 km SSMF. A slight performance improvement can be expected after 2.5 km SSMF.

To better understand the potential of the system in terms of high-bitrate transmission, achievable information rate (AIR) is subsequently plotted in Fig. 4, which is computed as $I_d R_s H$, where I_d is the value of the NGMI metric plotted in Fig. 3(a). The AIR values represent the maximum theoretical bitrate assuming an ideal code (i.e., a code with a rate I_d). For each PAM-m, m>2, we observe that an optimal symbol rate maximizing AIR was captured in the measured range. The optimal symbol rate decreases as the PAM order increases. Among all PAM orders, the highest AIR is obtained with 144 GBd PAM-8 signal, corresponding to a line rate of 432 Gbit/s and an AIR of 383.6 Gbit/s after 10 km SSMF transmission.

Next, net bitrate is computed considering two FEC schemes described in the previous section. For each NGMI threshold of the considered SD+HD concatenated codes in Table II, a corresponding horizontal line, which crosses the NGMI curves of different PAM signals in Fig. 3(a), can be plotted. Symbol rate, R_s', at the intersection of each threshold and each measured curve is interpolated, from which net bitrate is computed as $r_c R_s' H$, where r_c is the code rate corresponding to the specific NGMI threshold. The obtained net bitrates are subsequently recorded in Fig. 5(a) as a function of R_s'. For HD-only coding scheme, each BER threshold in Table II corresponds to a horizontal line in Fig. 3(b). Using the same approach as described above, the net bitrate is computed and recorded in Fig. 5(b). The obtained net bitrates in Fig. 5(a) follows the trend of the corresponding AIR curves in Fig. 4. Approximately 4% gap between net bitrate and

TABLE III
SUMMARY OF HIGHEST NET BITRATES AFTER 10 KM TRANSMISSION

FEC code	Modulation format	Net rate [Gbit/s]	Symbol rate [GBd]	Code rate[a] [–]
SD+HD concatenated (w/o and w/ puncturing)	PAM-2	189.7[b]	205.1[b]	0.9248
	PAM-3	233.1	172.3	0.9019
	PAM-4	287.1	156.2	0.9191
	PAM-6	329.9	147.2	0.8962
	PAM-8	363.4	143.7	0.8428
	Duobinary	218.8	247.3	0.8848
	Tribinary	256.1	283.9	0.9019
	Tetrabinary	279.0[b]	301.7[b]	0.9248
HD-only	PAM-2	193.4[b]	205.5[b]	0.9412
	PAM-3	227.0[b]	160.8[b]	0.9412
	PAM-4	286.9[b]	152.4[b]	0.9412
	PAM-6	318.0	143.1	0.8889
	PAM-8	311.2[b]	129.7[b]	0.8000
	Duobinary	216.7[b]	230.3[b]	0.9412
	Tribinary	253.9[b]	269.8[b]	0.9412
	Tetrabinary	277.1[b]	294.5[b]	0.9412

The results are extracted at the highest net bitrate of each curve for 10 km results in Figs. 5(a) and 8(a) for the SD+HD concatenated FEC and Figs. 5(b) and 8(b) for staircase FEC. [a]For the SD+HD concatenated FEC, code rate corresponds to the overall code rate from Table II. [b]Maximum was not attained over the measured range; the result may underestimate the performance.

AIR is due to the information loss of the considered SD+HD concatenated codes (0.04 is roughly the difference between rates of practical codes and the ideal code, having code rate equal to NGMI in Table II). Comparing the results of two FEC schemes in Fig. 5(a,b), the optimal symbol rate is lower when considering HD-only codes, except for binary modulation, for which the measured range failed to capture the optimum. For HD-only coding scheme, the optimal symbol rates of PAM-2, -3 and -4 signals are achieved with the lowest code rate, leaving space for improvement in case codes with similar information loss but lower BER threshold were available. In Table III, we summarize the highest net bitrates achieved using different orders of PAM with both FEC schemes after 10 km SSMF transmission. For SD+HD concatenated coding scheme, the highest net bitrate is 363.4 Gbit/s, possible with 143.7 GBd PAM-8 signal. A lower net bitrate can be achieved with HD-only coding scheme: the highest net bitrate of 318.0 Gbit/s is possible with a 143.1 GBd PAM-6 signal.

B. *Performance Evaluation of Polybinary Signaling*

The same performance evaluation procedure is carried out for polybinary signaling. Fig. 6(a,b) show NGMI and BER obtained with binary and various polybinary signals. Comparing at the same NGMI or BER threshold, the achievable symbol rate is improved using a signal with higher filter order n. This observation can be explained by the increasing polybinary spectral compression described in Section III.B. Symbol rates up to 304 GBd are measured applying tetrabinary modulation, arriving at NGMI values >0.96. In Fig. 7, AIR is plotted as a function of symbol rate. The highest AIR is 293.3 Gbit/s after 10 km SSMF, achieved with 304 GBd tetrabinary signal, corresponding to a line rate of 304 Gbit/s. Further improvement in AIR might be possible for tetrabinary modulation by increasing the symbol rate, even beyond 304 GBd.

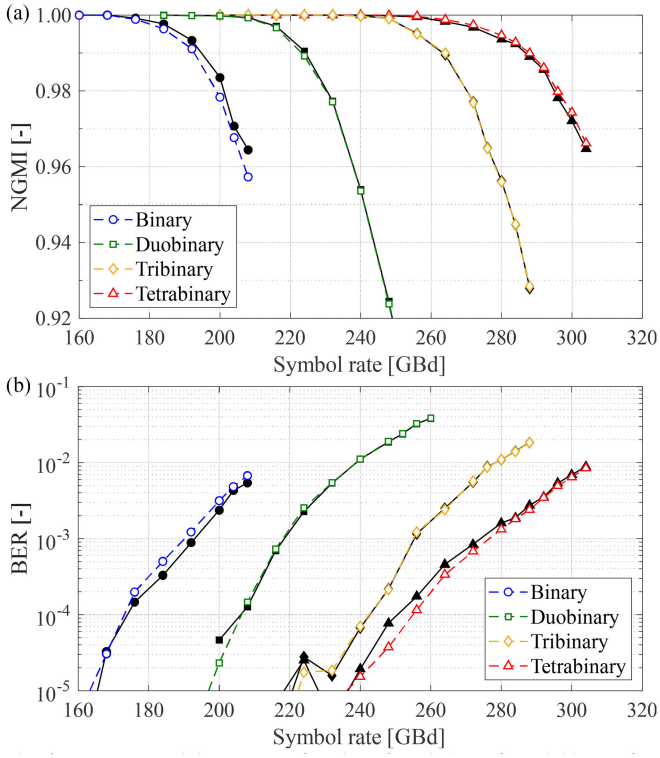

Fig. 6. (a) NGMI and (b) BER as a function of symbol rate for polybinary after 2.5 km (dashed colored lines) and 10 km (black continuous lines) SSMF transmission.

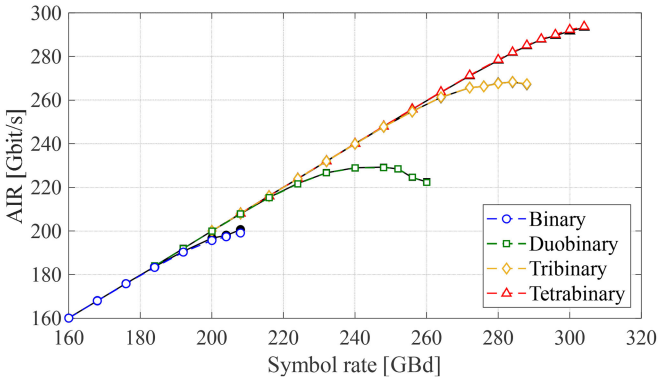

Fig. 7. AIR for polybinary after 2.5 km (dashed colored lines) and 10 km (black continuous lines) SSMF transmission.

Net bitrates obtained with both FEC schemes are plotted in Fig. 8. With SD+HD concatenated coding scheme, the optimal symbol rate maximizing the net bitrate increases with the filter order n in Fig. 8(a). For duobinary and tribinary modulation, an optimal symbol rate is captured in the measured range, while for binary and tetrabinary modulations, further increase in net bitrate is still possible by extending the range of measured symbol rates. With HD-only coding scheme in Fig. 8(b), the net bitrate is maximized for all modulation formats at the symbol rate corresponding to the lowest code rate of the considered codes. The best result for each polybinary modulation is tabulated in Table III. Comparing the results of the two FEC schemes,

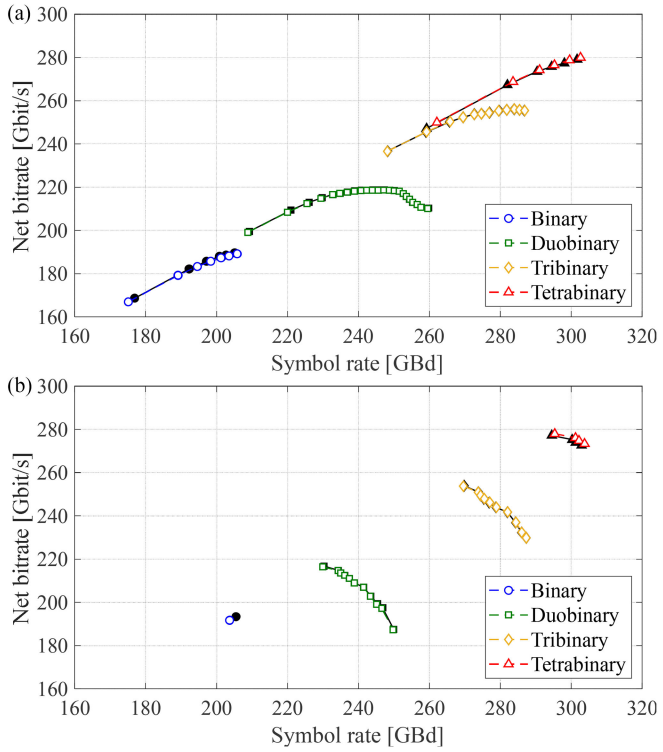

Fig. 8. Net bitrate achieved with: (a) SD+HD concatenated FEC and (b) HD-only FEC, as a function of symbol rate for polybinary after 2.5 km (dashed colored lines) and 10 km (black continuous lines) SSMF transmission.

HD-only coding leads to a small decrease (by a few Gbit/s) in the highest net bitrate of each polybinary modulation format, but requires a lower symbol rate to maximize the net bitrate. Among studied polybinary modulation formats, tetrabinary modulation is shown to be the best candidate to support a high-speed transmission: a net bitrate of 279.0 Gbit/s is obtained considering SD+HD concatenated coding scheme, and 277.1 Gbit/s considering HD-only coding scheme.

As demonstrated in this experiment, advanced IM/DD modulation formats give the possibility to realize higher net bitrates compared to a simple binary (PAM-2) modulation. When comparing PAM-m, m>2, to polybinary modulation, the former yields higher net bitrates at lower symbol rates due to its higher source entropy. Although polybinary modulation does not outperform PAM in the scenario of achieving the highest net bitrate considered in this paper, this does not completely rule out polybinary as a potential modulation format for optical interconnects. Other aspects of polybinary modulation which are not studied here, such as dispersion tolerance, may be advantageous in certain scenarios.

V. Conclusion

By employing an ultrabroad-bandwidth plasmonic MZM with micrometer footprint, an ultrahigh-net-bitrate IM/DD system is experimentally demonstrated. PAM and polybinary modulation formats of different orders are evaluated in terms of practically achievable net bitrates, considering an SD+HD concatenated FEC coding scheme and an HD-only FEC coding scheme. Applying PAM modulation, we successfully demonstrate a net bitrate of 363.4 Gbit/s after 10 km SSMF transmission considering the former FEC scheme, and a net bitrate of 317.98 Gbit/s considering the latter FEC scheme. With polybinary modulation, a symbol rate exceeding 300 GBd is demonstrated, leading to a net bitrate of 279.0 Gbit/s with the former, and 277.1 Gbit/s with the latter, leaving an unexplored margin to further improve this result.

Acknowledgment

Polariton Technologies Ltd. would like to thank the Binnig and Rohrer Nanotechnology Center (BRNC).

References

[1] J. D'Ambrosia, "The case for 1.6 terabit Ethernet," IEEE 802.3 Beyond 400 Gb/s Ethernet Study Group, May 2021. Accessed: Sep. 3, 2021. [Online]. Available: https://www.ieee802.org/3/B400G/public/21_05/dambrosia_b400g_01b_210524.pdf

[2] C. Minkenberg, R. Krishnaswamy, A. Zilkie, and D. Nelson, "Co-packaged datacenter optics: Opportunities and challenges," *IET Optoelectron.*, vol. 15, no. 2, pp. 77–91, 2021.

[3] X. Zhou, R. Urata, and H. Liu, "Beyond 1 Tb/s intra-data center interconnect technology: IM-DD or coherent?," *J. Lightw. Technol.*, vol. 38, no. 2, pp. 475–484, Jan. 2020, doi: 10.1109/JLT.2019.2956779.

[4] N. P. Diamantopoulos *et al.*, ">100-GHz bandwidth directly-modulated lasers and adaptive entropy loading for energy-efficient >300-Gbps/λ IM/DD systems," *J. Lightw. Technol.*, vol. 39, no. 3, pp. 771–778, Feb. 2021, doi: 10.1109/JLT.2020.3021727.

[5] S. Yamaoka *et al.*, "Directly modulated membrane lasers with 108 GHz bandwidth on a high-thermal-conductivity silicon carbide substrate," *Nature Photon.*, vol. 15, pp. 28–35, 2021, doi: 10.1038/s41566-020-00700-y.

[6] D. Che *et al.*, "Long-term reliable >200-Gb/s directly modulated lasers with 800GbE-compliant DSP," in *Proc. Opt. Fiber Commun. Conf. Exhibit.*, 2021, pp. 1–3.

[7] J. Zhou, J. Wang, L. Zhu, and Q. Zhang, "High baud rate all-silicon photonics carrier depletion modulators," *J. Lightw. Technol.*, vol. 38, no. 2, pp. 272–281, Jan. 2020, doi: 10.1109/JLT.2019.2933384.

[8] J. M. Estarán *et al.*, "140/180/204-Gbaud OOK transceiver for inter- and intra-data center connectivity," *J. Lightw. Technol.*, vol. 37, no. 1, pp. 178–187, Jan. 2019, doi: 10.1109/JLT.2018.2876732.

[9] S. Kanazawa *et al.*, "214-Gb/s 4-PAM operation of flip-chip interconnection EADFB laser module," *J. Lightw. Technol.*, vol. 35, no. 3, pp. 418–422, Feb. 2017, doi: 10.1109/JLT.2016.2632164.

[10] M. S. B. Hossain *et al.*, "402 Gb/s PAM-8 IM/DD O-band EML transmission," in *Proc. 47th Eur. Conf. Opt. Commun.*, 2021, pp. 1–4, doi: 10.1109/ECOC52684.2021.9605884.

[11] G. W. Lu *et al.*, "High-temperature-resistant silicon-polymer hybrid modulator operating at up to 200 Gbit s^{-1} for energy-efficient datacentres and harsh-environment applications," *Nature Commun.*, vol. 11, 2020, Art. no. 4224, doi: 10.1038/s41467-020-18005-7.

[12] C. Wang *et al.*, "Integrated lithium niobate electro-optic modulators operating at CMOS-compatible voltages," *Nature*, vol. 562, pp. 101–104, 2018, doi: 10.1038/s41586-018-0551-y.

[13] C. Haffner *et al.*, "Plasmonic organic hybrid modulators – scaling highest-speed photonics to the microscale," *Proc. IEEE*, vol. 104, no. 12, pp. 2362–2379, Dec. 2016, doi: 10.1109/JPROC.2016.2547990.

[14] B. Baeuerle *et al.*, "Reduced equalization needs of 100 GHz bandwidth plasmonic modulators," *J. Lightw. Technol.*, vol. 37, no. 9, pp. 2050–2057, May 2019, doi: 10.1109/JLT.2019.2897480.

[15] W. Heni *et al.*, "Ultra-high-speed 2:1 digital selector and plasmonic modulator IM/DD transmitter operating at 222 GBaud for intra-datacenter applications," *J. Lightw. Technol.*, vol. 38, no. 9, pp. 2734–2739, May 2020, doi: 10.1109/JLT.2020.2972637.

[16] Q. Hu *et al.*, "Plasmonic-MZM-based short-reach transmission up to 10 km supporting >304 GBd polybinary or 432 Gbit/s PAM-8 signaling," in *Proc. 47th Eur. Conf. Opt. Commun.*, 2021, pp. 1–4, doi: 10.1109/ECOC52684.2021.9606060.

[17] P. Kabal and S. Pasupathy, "Partial-response signaling," *IEEE Trans. Commun.*, vol. 23, no. 9, pp. 921–934, Sep. 1975, doi: 10.1109/TCOM.1975.1092918.

[18] E. Kretzmer, "Generalization of a techinque for binary data communication," *IEEE Trans. Commun. Technol.*, vol. 14, no. 1, pp. 67–68, Feb. 1966, doi: 10.1109/TCOM.1966.1089288.

[19] R. Howson, "An analysis of the capabilities of polybinary data transmission," *IEEE Trans. Commun. Technol.*, vol. 13, no. 3, pp. 312–319, Sep. 1965, doi: 10.1109/TCOM.1965.1089138.

[20] Q. Wu, Y. Zhu, L. Yin, and W. Hu, "50 Gbaud PAM-4 IM-DD transmission with 24% bandwidth compression based on polybinary spectral shaping," in *Proc. 47th Eur. Conf. Opt. Commun.*, 2021, pp. 1–4, doi: 10.1109/ECOC52684.2021.9606146.

[21] W. Heni *et al.*, "108 Gbit/s plasmonic Mach–Zehnder modulator with >70-GHz electrical bandwidth," *J. Lightw. Technol.*, vol. 34, no. 2, pp. 393–400, Jan. 2016, doi: 10.1109/JLT.2015.2487560.

[22] W. Heni *et al.*, "Nonlinearities of organic electro-optic materials in nanoscale slots and implications for the optimum modulator design," *Opt. Exp.*, vol. 25, no. 3, pp. 2627–2653, Feb. 2017, doi: 10.1364/OE.25.002627.

[23] H. Xu *et al.*, "Ultrahigh electro-optic coefficients, high index of refraction, and long-term stability from Diels-Alder cross-linkable binary molecular glasses," *Chem. Mater.*, vol. 32, no. 4, pp. 1408–1421, Jan. 2020, doi: 10.1021/acs.chemmater.9b03725.

[24] A. Melikyan *et al.*, "High-speed plasmonic phase modulators," *Nature Photon.*, vol. 8, pp. 229–233, Feb. 2014, doi: 10.1038/nphoton.2014.9.

[25] W. Heni *et al.*, "Plasmonic IQ modulators with attojoule per bit electrical energy consumption," *Nature Commun.*, vol. 10, 2019, Art. no. 1694, doi: 10.1038/s41467-019-09724-7.

[26] M. Burla *et al.*, "500 GHz plasmonic Mach–Zehnder modulator enabling sub-THz microwave photonics," *APL Photon.*, vol. 4, no. 5, 2019, Art. no. 056106, doi: 10.1063/1.5086868.

[27] C. Haffner *et al.*, "Harnessing nonlinearities near material absorption resonances for reducing losses in plasmonic modulators," *Opt. Mater. Exp.*, vol. 7, no. 7, pp. 2168–2181, Jul. 2017, doi: 10.1364/OME.7.002168.

[28] R. D. Wesel, X. Liu, J. M. Cioffi, and C. Komninakis, "Constellation labeling for linear encoders," *IEEE Trans. Inf. Theory*, vol. 47, no. 6, pp. 2417–2431, Sep. 2001, doi: 10.1109/18.945255.

[29] J. Cho and L. Schmalen, "Construction of protographs for large-girth structured LDPC convolutional codes," in *Proc. IEEE Int. Conf. Commun.*, 2015, pp. 4412–4417, doi: 10.1109/ICC.2015.7249017.

[30] S. ten Brink, "Convergence behavior of iteratively decoded parallel concatenated codes," *IEEE Trans. Commun.*, vol. 49, no. 10, pp. 1727–1737, Oct. 2001, doi: 10.1109/26.957394.

[31] T. Tian, C. R. Jones, J. D. Villasenor, and R. D. Wesel, "Selective avoidance of cycles in irregular LDPC code construction," *IEEE Trans. Commun.*, vol. 52, no. 8, pp. 1242–1247, Aug. 2004, doi: 10.1109/TCOMM.2004.833048.

[32] A. Suls, Y. Lefevre, J. Van Hecke, M. Guenach, and M. Moeneclaey, "Error performance prediction of randomly shortened and punctured LDPC codes," *IEEE Commun. Lett.*, vol. 23, no. 4, pp. 560–563, Apr. 2019, doi: 10.1109/LCOMM.2019.2900893.

[33] L. M. Zhang and F. R. Kschischang, "Staircase codes with 6% to 33% overhead," *J. Lightw. Technol.*, vol. 32, no. 10, pp. 1999–2002, May 2014, doi: 10.1109/JLT.2014.2316732.